THE JOURNAL OF PHYSICAL CHEMISTRY B

pubs.acs.org/JPCB Article

Evolution of Hydrogen-Bond Interactions within Single Levitated Metastable Aerosols Studied by In Situ Raman Spectroscopy

Pyeongeun Kim, Wei Xiong, and Robert E. Continetti*

Cite This: J. Phys. Chem. B 2020, 124, 9385−9395 Read Online

ACCESS | Metrics & More | Article Recommendations | Supporting Information

ABSTRACT: Atmospheric aerosols can exist as supersaturated (metastable) liquid or glassy states, with physical and chemical properties that are distinct from the solid or liquid phases. These unique properties of aerosols have substantial implications on climate and health effects. Direct investigations on metastable aerosols remain a challenge because any interfacial contact can cause heterogeneous nucleation. In this study, in situ Raman spectroscopic and Mie scattering imaging analysis is applied to metastable aerosols in the absence of physical contact using an environment-controlled electrodynamic balance (EDB). This has allowed a detailed study of the O−H stretching regions of the Raman spectrum, revealing evidence for the rearrangement of hydrogen-bonding structures of levitated aqueous citric acid (CA) and aqueous sucrose droplets at metastable liquid states. We found that carboxyl groups in a CA droplet yield distinctive dynamics of strong and weak hydrogen bonds, whereas hydroxyl groups in a sucrose droplet show correlated strong and weak interactions. Such effects are particularly important in a supersaturated solution. These results indicate that metastable liquid aerosols from different sources may exhibit distinct physical and chemical behavior.

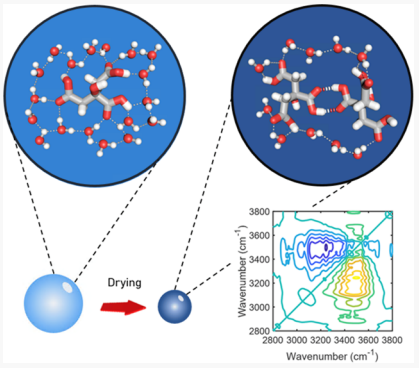

1. INTRODUCTION

Atmospheric aerosols are of great interest because of their significant impacts on the environment and human health by affecting the climate through radiative forcing, providing reaction sites for heterogeneous chemistry, and causing respiratory and cardiovascular diseases.[1,2] Recent studies have shown the viability of pathogenic bacteria and viruses in the aerosol form, including SARS-CoV-2, which is known to cause coronavirus disease 2019 (COVID-19).[3−5] Therefore, it is important to understand the unique physical and chemical properties of atmospheric aerosols that often differ from bulk properties of the same compounds, e.g., owing to the large surface to volume ratio and high supersaturation. Organic aerosols (OAs) can be emitted directly from the source (primary OAs) or produced by a series of oxidative reactions (secondary OAs). It has been discovered that OAs can exist as metastable liquid as well as amorphous solid (glassy) droplets.[6−8] This range of phenomena poses a significant difficulty for treating atmospheric aerosols in climate models because current models assume that aerosols are in thermodynamically equilibrated liquid or solid states.[9] Moreover, recent studies have revealed phase separation and kinetic limitations for diffusion within highly supersaturated and glassy OAs, which are nonequilibrium phenomena mediated by intermolecular interactions, including hydrogen bonding.[10,11] These results have substantial ramifications on the physical and chemical properties of atmospheric aerosols, such as water uptake, heterogeneous chemical reactions, ice nucleation, and long-range transport of toxic pollutants.[12−14] To provide further insights into these systems, the present study examines fundamental molecular interactions in supersaturated OAs, focusing on the hydrogen-bonding network in these aerosols as a function of relative humidity.

Primary and secondary OAs can undergo oxidative reactions, forming less volatile and more hygroscopic oxygenated organic aerosols (OOAs).[15] To understand the unique properties of supersaturated OOAs, it is critical to characterize the hydrogen-bond interactions within them. In supersaturated OOAs, water acts as a bonding media between organic molecules and leads to significant intermolecular interactions through hydrogen bonds. Hydrogen-bond interactions manifest themselves in macroscopic properties of OOAs such as phase state, viscosity, nucleation, and cloud condensation.[16] Although a water molecule has a simple structure, liquid water forms complex local structures, due to extensive hydrogen-bond networks. Vibrational spectroscopy (Fourier transform infrared (FTIR) or Raman) is a powerful experimental tool to unravel such intricate hydrogen-bond interactions because of their sensitivity to O−H stretching vibrations. Studies on these topics have provided insights into the structure of water at

Received: May 31, 2020
Revised: September 22, 2020
Published: September 22, 2020

https://dx.doi.org/10.1021/acs.jpcb.0c04919
J. Phys. Chem. B 2020, 124, 9385−9395

ambient to extreme conditions,[17−19] effects of ions on the structure of water,[20−22] and hydrogen-bond interactions in organic−water systems.[23]

Aqueous citric acid (CA) and aqueous sucrose droplets were chosen as model OOAs. They are common compounds in OOAs, and they both exhibit the ability to form glassy states under certain conditions.[14,24,25] In the form of an aqueous droplet, both CA−water and sucrose−water systems can exist in a supersaturated state at ambient temperature.[26] However, in detail, the hydrogen-bond interactions in these two systems differ considerably because CA and sucrose have distinctive hydrophilic functional groups, i.e., CA is a tricarboxylic acid with one hydroxyl group and sucrose is a disaccharide containing eight hydroxyl groups and three ether groups (Figure 1). In dilute aqueous solution, the difference of the

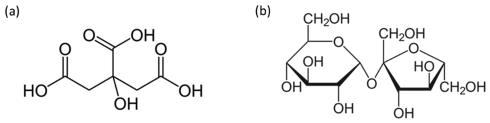

Figure 1. Molecular structure of citric acid (a) and sucrose (b).

solute effects on hydrogen-bond interactions may be minute as both solutes only disturb the local water−water interactions through solvation. The dissimilarity arises in high solute supersaturation as the fractions of solutes in the aqueous droplet become significant, and solute−solute interactions become increasingly important. Thus, it is expected that the different structures of the hydrophilic groups in these solutes can lead to differences in the hydrogen-bond interactions in aqueous CA and aqueous sucrose droplets in highly supersaturated OOAs.

Contact-free levitation is a key condition in the investigations reported here because heterogeneous nucleation sites, such as surface contact, can trigger crystallization of metastable droplets. Aerosol optical tweezer (AOT) and electrodynamic balance (EDB) instruments are commonly used to confine single microdroplets in a contact-free manner.[27] AOT traps a single spherical droplet at the center of a tightly focused laser beam by balancing gravity with the photon gradient force. AOTs have been used in aerosol chemistry and physics, including studies of chemical kinetics,[28] hygroscopicity,[29] optical properties,[26] and water diffusion.[30] EDB is another widely used technique in aerosol research, making use of a combination of AC and DC electric fields to confine single-charged droplets.[31] The levitation ability of EDBs is not limited by size or morphology. Thus, EDB can effectively perform studies involving phase transitions or nucleation.[32,33]

In spite of a number of theoretical investigations on understanding hydrogen-bond structures in atmospheric aerosols, there has been a lack of laboratory studies.[16,34] The present work uses an environment-controlled EDB to trap single-model OOAs (CA or sucrose) for study with in situ Raman and Mie scattering spectroscopy. Integration of these techniques with the EDB allows measuring the spectroscopic signatures of hydrogen bonding in metastable liquid OOAs. The Raman spectra of single droplets as a function of relative humidity (RH) were obtained. Mie scattering image analysis was used to probe the size and phase state of the droplet under study. The Raman spectral region of 3000−3800 cm^{-1} (O−H stretch band, ν(O−H)) upon evaporation was primarily analyzed using Gaussian deconvolution as well as a two-dimensional (2D) correlation method. The 2D correlation method provides a great advantage in this study because of the sensitivity to asynchronous intensity changes in different spectral regions, which are often overlooked by conventional spectrum analysis.[35,36] Thus, the 2D correlation method enables a detailed description of the evolution of the intermolecular hydrogen-bond interactions in these systems. A combination of linear and 2D spectral analysis clearly shows the evidence of different hydrogen-bond dynamics within CA and sucrose droplets. It was found that the persistence of local hydrogen-bond interactions is determined by the functional groups of the solute, especially at high supersaturation. The results imply that carboxylic groups in CA lead to the sequential evolution of strong and weak hydrogen-bond interactions as evaporation of a metastable CA droplet occurs. On the other hand, hydrogen-bond interactions in a sucrose droplet display correlated network-like behavior.

2. EXPERIMENTAL METHODS

2.1. Single-Particle Confinement and In Situ Spectroscopic Techniques. The environment-controlled EDB with Mie and Raman spectroscopy setup has been previously described in detail.[11] The schematic layout of the EDB system is shown in Figure 2. In brief, a combination of AC and DC

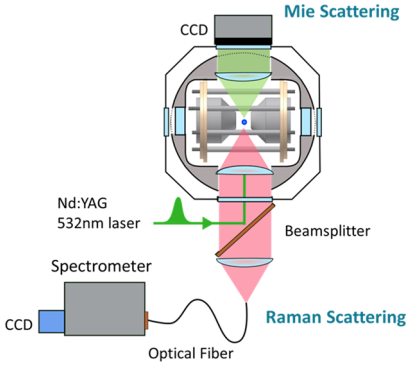

Figure 2. Electrodynamic balance (EDB) apparatus setup with Raman and Mie spectroscopy. A droplet is located at the center of the trap (blue dot). A 532 nm pulsed laser is focused on the droplet generating an elastic Mie scattering pattern (green shade) and inelastic Raman scattering signal (red shade).

voltages from conical endcaps and 8 rod electrodes confines a single-charged droplet at the null point of the trap. An inductive charging ring and a grounded piezoelectric tip charge the droplets. The principle and applications of EDB have been well established.[37,38] The trapped droplet was irradiated by a pulsed 532 nm Nd:YAG laser beam (RPMC Wedge XF, 3.5 μs pulse width, 80 kHz repetition rate) with ∼25 mW average power. The back-scattered Raman signal with all polarizations was collected through a fiber optic coupled into a spectrometer (Acton SpectraPro 275, f/3.8) equipped with a 600 g/mm grating and an open-electrode TE-cooled CCD detector (Horiba Syncerity). The exposure time was 30−60 s, and two spectra at each RH were averaged to obtain the high signal to noise ratio spectra for the single droplets. The effective spectral resolution was ∼6 cm^{-1}. Spectrometer calibration was done using four strong Raman peaks of solid naphthalene (764, 1382, 1577, and 3056 cm^{-1}).[39] The forward scattered (45°) Mie scattering pattern was collected using a CCD camera with the 16.3° solid angle. Typical diameters of the

https://dx.doi.org/10.1021/acs.jpcb.0c04919
J. Phys. Chem. B 2020, 124, 9385−9395

droplets determined by analysis of the Mie scattering patterns were 40−60 μm, with the analysis carried out as described in ref 11 and an earlier study.[40,41] Based on previous studies, the surface charge density of the droplet in this work (<40 elementary charges per μm^2) was assumed to have only negligible effects on the Raman spectra.[11,42,43]

Aqueous solutions were prepared by dissolving citric acid (99% purity, Macron Fine Chemicals) and sucrose (99.9% purity, Fisher) in deionized water. Typical initial concentrations of both solutions before injection into the trap were 1.5−2.0 M. Measurements were made over the RH range between 88 and 0.6% (±1.5%) as determined using a capacitive humidity sensor (Vaisala Humicap 180R). The relative humidity inside the trap was controlled by a bubbler system consisting of digital mass flow controllers (Alicat MC-500SCCM) coupled with dry and humid N_2. Both droplets are expected to have concentration inhomogeneity at a lower RH region due to the slow diffusion rate of water (RH 11% and below for CA and 52% and below for sucrose). The inner concentration gradient of the droplets is modeled using the kinetic multilayer model by Zobrist et al. and described in detail in Supporting Information, Figure S1. The Raman spectra collected at nonequilibrium conditions represent an ensemble average of molecular vibrations of the droplets, not accountable for concentration gradient. All measurements were made at ambient temperature (19−21 °C). Over the entire RH range studied here, the Mie scattering images for both CA and sucrose droplets exhibited regular diffraction patterns, indicating that the droplets maintained spherically symmetric metastable liquid states without noticeable phase transition during these studies. The Raman spectrum of neat water was obtained using a cuvette holder with an optical fiber adapter (Thorlabs CVH100) located in the laser path past the EDB.

2.2. Raman Spectrum of Liquid Water: O−H Stretching Modes. The Raman spectrum of liquid water, especially the broadband of the O−H stretching region (ν(O−H); 2800−3800 cm^{-1}), is of great interest, and many studies have attempted to explain its unique spectral characteristics.[17,19,44,45] In the present study, this feature is examined using a conventional three-Gaussian peak deconvolution of the ν(O−H) band.[21,46,47] For analysis of the liquid phase Raman spectra, Gaussians are commonly used because complex interactions between O−H oscillators lead to an inhomogeneous broadening of the spectral lineshape.[48] Figure 3 shows the Raman spectrum of bulk liquid water in the ν(O−H) region and its three-Gaussian fit. Following the generally accepted peak assignments, the broad ν(O−H) band of liquid water consists of a strong hydrogen-bond peak (~3250 cm^{-1}), a weak hydrogen-bond peak (~3450 cm^{-1}), and the weakest hydrogen-bond or nonbonded O−H (~3650 cm^{-1}) peak.[21,49] As a general principle in the harmonic oscillator approximation for the O−H stretching oscillators, hydrogen-bond interactions alter the force constants of the oscillators leading to the peak frequency shifts (stronger interactions lower the force constant and frequency and vice versa). In Figure 3, the first two peaks at ~3250 and ~3450 cm^{-1} have a notably higher intensity than the nonbonded O−H peak (~3650 cm^{-1}). The overall shape of the ν(O−H) band transforms in response to physical (temperature and pressure)[17,18,44,50,51] and chemical (concentration and character of solutes)[20−23,52] perturbations due to changes in the hydrogen-bonding structure. In the present study, the evolution of strong and weak hydrogen-bond interactions represented by the peaks at ~3250 and ~3450 cm^{-1} of CA−water and sucrose−water systems is examined.

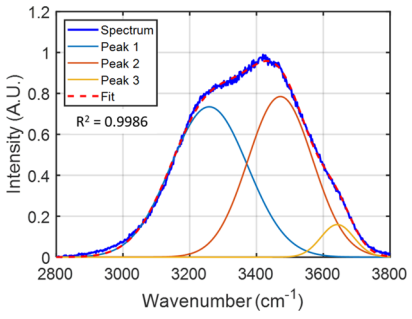

Figure 3. Raman spectrum of the O−H stretching band of neat liquid water at 20 °C. Three Gaussian peaks are applied to represent different hydrogen-bond interactions: peak 1 as strong, peak 2 as weak, and peak 3 as weakest (nonbonded O−H).

2.3. 2D Correlation Analysis. The 2D correlation method for linear IR spectrum analysis was first introduced by Noda and has been widely used in various applications, including analysis of the structure of water, protein structure and dynamics, and studies of the catalytic mechanisms.[19,35,36,53] In 2D correlation analysis, spectral data are treated as matrices, as described by eq 1

$$\tilde{\mathbf{X}}(\nu) = \begin{bmatrix} \tilde{x}(\nu,\ t_1) \\ \tilde{x}(\nu,\ t_2) \\ \vdots \\ \tilde{x}(\nu,\ t_m) \end{bmatrix} \tag{1}$$

where ν is a spectral variable (wavenumber), t_m is the external variable, and m is the number of the spectra at a given range of external perturbation (RH). $\tilde{x}$ is the dynamic spectrum defined by the difference between the raw and reference spectra, which is referred to as the dynamic spectrum $\tilde{x}(\nu, t)$,

$$\tilde{x}(\nu, t) = x(\nu, t) - \bar{x}(\nu) \tag{2}$$

where $\bar{x}(\nu)$ is the reference spectrum chosen in this study to be the spectrum at a chosen RH (67% for CA and 60% for sucrose). These RH points were chosen because the spectral intensities in the linear spectra exhibit more subtle changes at lower RH, making the 2D correlation method more useful in the analysis. Using a matrix notation for the dynamic spectrum of the system under study, the synchronous 2D correlation spectrum is obtained by

$$\mathbf{\Phi}(\nu_1, \nu_2) = \frac{1}{m-1}\tilde{X}(\nu_1)^T\tilde{X}(\nu_2) \tag{3}$$

Following Noda, the asynchronous 2D correlation spectrum can be described as

$$\boldsymbol{\psi}(\nu_1, \nu_2) = \frac{1}{m-1}\tilde{\mathbf{X}}(\nu_1)^{\mathrm{T}}\mathbf{N}\tilde{\mathbf{X}}(\nu_2) \tag{4}$$

where $\mathbf{N}$ is the Hilbert−Noda transformation matrix that orthogonalizes the matrix of the experimental data.[54] Equations 3 and 4 are generalizations of 2D correlation spectroscopy. In the results presented here, this method will be applied to understanding the evolution of the Raman spectra as RH decreases. All data analysis was carried out using Matlab (Mathworks, Naticks).

https://dx.doi.org/10.1021/acs.jpcb.0c04919
J. Phys. Chem. B 2020, 124, 9385−9395

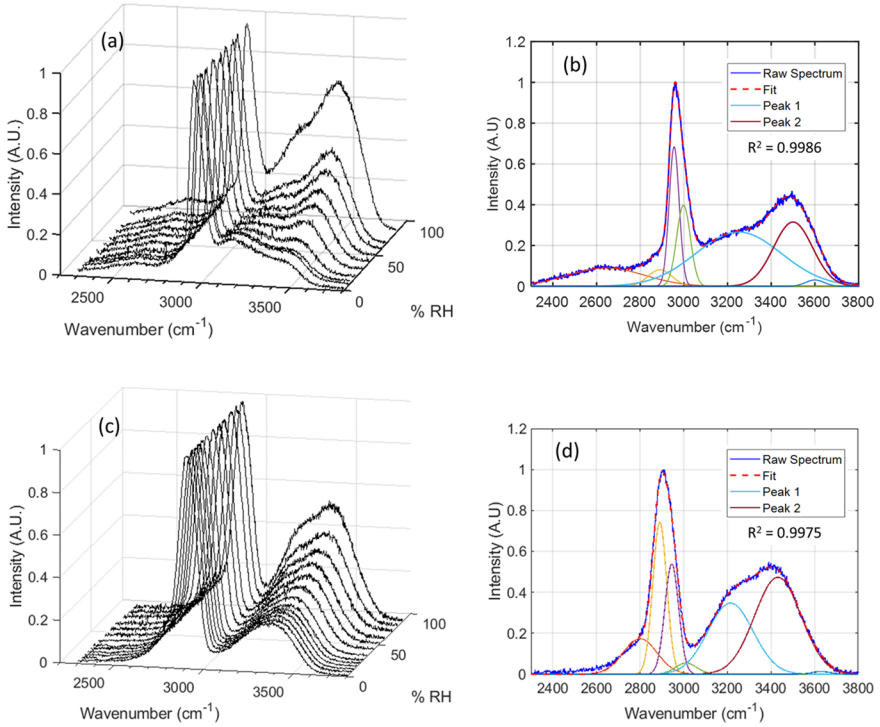

Figure 4. (a) Raman spectra of aqueous CA droplet versus RH. (b) Gaussian deconvolution of the Raman spectrum of the CA droplet at 67% RH. Peak assignments are as follows: ~2600 cm^{-1}: ν(O−H) with the strongest hydrogen bond, ~2950 cm^{-1}: ~2880 cm^{-1}: combinational, ν(C−H), ~3250 cm^{-1} (peak 1): ν(O−H) with the strong hydrogen bond, ~3500 cm^{-1} (peak 2): ν(O−H) with the weak hydrogen bond, and ~3600 cm^{-1}: nonbonded ν(O−H). Frames (c) and (d) show the Raman spectra of the aqueous sucrose droplet and its Gaussian deconvolution. Peak assignments for sucrose droplet are ~2800 cm^{-1}: combinational, ~2950 cm^{-1}: ν(C−H), ~3250 cm^{-1} (peak 1): ν(O−H) with the strong hydrogen bond, ~3450 cm^{-1} (peak 2): ν(O−H) with the weak hydrogen bond, and ~3630 cm^{-1}: nonbonded ν(O−H). Complete sets of the fitting parameters are available in Supporting Information, Tables S2 and S3.

3. RESULTS

In the following, first, the Raman spectra of the aqueous CA and sucrose droplets as a function of RH will be presented, followed by examining the peak shifts observed as the droplets are dried and reach extreme levels of supersaturation. The 2D correlation analysis of the spectral changes will then be presented.

In situ Raman spectra of aqueous CA and aqueous sucrose droplets are described below.

3.1. Citric Acid Droplets. A set of 10 Raman spectra of the aqueous CA droplet versus decreasing RH (from 82% down to 1%) are shown in Figure 4a. All Mie scattering images obtained over the course of the experiment showed a regular fringe pattern (Figure S2), indicating that the droplet did not crystallize even at 1% RH, instead persisting as a spherically symmetric metastable liquid.[26] The wavenumber range of interest (2300−3800 cm^{-1}) consists of multiple narrow and wide peaks. Figure 4b shows one example of the Gaussian deconvolution of a droplet Raman spectrum. Seven Gaussian components were used to represent different vibrational modes in the spectra. The ν(C−H) peak near 2950 cm^{-1} is minimally affected by RH, and thus it is used to normalize the spectral intensities over the measurements. As the droplet loses water content, the total number of O−H oscillators decreases, accompanied by a reduction in the overall intensity of the ν(O−H) bands from 3000 to 3800 cm^{-1}. However, the intensity does not decrease at a uniform rate across the band because the aqueous CA droplet Raman signature contains several distinct O−H oscillators, including the carboxyl group (R−COOH), the hydroxyl group (R−OH), and the water solvent (HOH). These features evolve differently in the drying environment. To study evolution of the hydrogen-bond interactions as a function of RH, it is necessary to deconvolute the Raman spectrum in the Gaussian peaks assigned to the various O−H containing functional groups.

Compared to the Raman spectrum of water (Figure 3), the spectrum of CA (Figure 4b) has unique features. First, the weak and broad shoulder at ~2600 cm^{-1} shows negligible intensity change during the evaporation of water. Given that this broad shoulder peak is not observed in the sucrose spectrum (Figure 4d), it can be considered as a unique interaction of the carboxylic acid and water. An ab initio study on hydrated acetic acid showed the strong hydrogen-bond of the water-bridged acetic acid dimer, which leads to the vibrational wavenumber at ~2750 cm^{-1}.[55] Thus, this broad shoulder peak can be assigned as the strongest water−CA hydrogen-bond interaction that is least affected by the evaporation of water. Similar strong hydrogen-bond interactions were also observed recently in biomimetic self-assemblies by vibrational sum frequency generation spectroscopy.[56] Second, the width of assigned peak 1 in the CA spectrum is larger than in the water or sucrose spectrum. According to vibrational spectroscopic studies on various carboxylic acids, small Raman peaks of the acidic O−H stretch lie in the 2800−3100 cm^{-1} range as weak shoulders on the strong C−H stretch peak (~2950 cm^{-1}).[57−59] Therefore, peak 1 contains acidic O−H character from CA along with the major contribution from water solvent.

The evolution of the hydrogen-bond structures during evaporation of the CA droplet is evident in the overall shape

https://dx.doi.org/10.1021/acs.jpcb.0c04919
J. Phys. Chem. B 2020, 124, 9385−9395

change of the ν(O−H) band. Qualitatively, at the beginning of the measurement (82% RH), the weak hydrogen-bonding peak at ∼3500 cm^{-1} (peak 2) is more intense than the strong hydrogen-bonding peak at ∼3250 cm^{-1} (peak 1). In contrast, at the end of the measurement (1% RH), peak 1 is the dominant hydroxyl feature in the spectrum. This change can be explained by the interaction of CA and the water molecule. Interactions of water molecules in the CA−water solution system can be classified into two broad classes: direct participation in the hydration of CA (first shell of solvent molecules) or only weakly (or not) engaged in the hydration of CA. Stronger hydrogen-bond interaction is expected when the water molecules are in the first hydration shell of CA due to the stronger C═O···H−O interaction compared to water−water interactions by ∼1 kcal/mol.[60,61] As the strong hydrogen bond red-shifts the vibrational frequency, one can assume that a large contribution to peak 1 comes from water molecules in the first hydration shell and peak 2 has the character of water molecules outside of the hydration shell.

The different decreasing rates of the peaks 1 and 2's intensities upon dehumidifying support this assignment. As the droplet evaporates, the increase in the concentration of CA diminishes the probability of water−water interactions (peak 2) compared to direct water−CA interactions (peak 1), thus the overall intensity decrease is faster for peak 2. The decrease in intensity of peak 1, however, plateaus below 67% RH in spite of continuous evaporation of water. This behavior reinforces the hypothesis that peak 1 mainly originates from the water molecules in the first hydration shell. Given that the CA droplet maintained a spherically symmetric liquid state, as determined by Mie scattering, even under the driest conditions, it can be inferred that the CA molecules must stay hydrated to a certain level. These observations are consistent with spectroscopic studies that have shown stronger hydrogen bonding in C═O···H−O interaction compared to H−O···H−O, as determined by spectral red shifts.[58,61,62]

3.2. Sucrose Droplets. Raman measurements on the aqueous sucrose droplets have also been made over the range from 88% down to 1% RH. Thirteen Raman spectra as a function of RH are shown in Figure 4c, exhibiting distinct spectral evolution compared to a CA droplet. At a glance, the intensities of all peaks decrease at similar rates as RH decreases. Figure 4d shows an example of the Gaussian deconvolution for sucrose. As seen in CA, the nonbonded ν(O−H) peak rapidly diminishes below 60% RH. The water−sucrose system contains hydroxyl groups (−OH), ether groups (−O−), and the water solvent (HOH). These different functional groups lead one to expect different structural evolution as supersaturation increases compared to the water−CA system. It is notable that the hydrogen-bond interaction between sucrose−water (hydroxyl OH−water) is energetically closer to the water−water interaction than CA−water (acidic OH−water).[61,63,64] This means that in a sucrose droplet, the formation of a strongly bound first hydration shell is not expected, and a randomized network-like liquid structure is expected to be maintained. Therefore, the overall intensity of the O−H band shows a commensurate decrease of both peaks upon evaporation, maintaining a balanced population ratio of the strong to weak hydrogen bonds. Thus, the hydroxyl groups of sucrose and the water molecules contribute almost equally to the Raman ν(O−H) spectral feature within the sucrose droplet. The striking dissimilarity of the spectral intensity changes between CA and sucrose droplets provides qualitative insight into the hydrogen-bond interactions in these distinct solute systems.

3.3. Quantitative Analysis of Spectral Peak Shifts. In addition to the characteristic intensity changes of peak 1 and 2 of the CA and the sucrose droplets discussed earlier, the frequency shifts of the peaks provide further information on the hydrogen-bond interactions. The strength of the intermolecular interactions of the O−H ensembles can be probed by examination of the blue- or red shift of the peaks as a function of RH. The frequency shift of peak 1 and peak 2 of CA and the sucrose droplets as a function of RH is shown in Figure 5. The unitless supersaturation ratio S is defined by $S = C/C_e$, where C is the solute concentration of the droplet and C_e is the molar concentration of the solution at the saturation point (C_e (CA) = 3.08 and C_e (sucrose) = 1.95).[65,66] At each RH measurement, values of S and the water mole fraction (x_w) have been calculated using the measured volume of the droplet (equilibrium RHs) and a kinetic model with existing parametrization from the literature.[14,67] Values of S increase from 1.2 to 2.6 for CA and 1.2 to 2.0 for sucrose as the droplets evaporate (data for RH versus S and x_w are available in Table S1). For the CA droplet, peak 1 shows a steady red shift down to 10% RH. This frequency shift is consistent with increasingly strong hydrogen-bond interactions as the droplet evaporates and equilibrates to a higher concentration. Below 10% RH, an abrupt diminution in the red shift of peak 1 in this region is observed. The red shift of peak 2 in CA exhibits a sudden change at high supersaturation (RH < 20%). This suggests that these different rates of frequency shift are related to the dependence of the distribution of hydrogen bonds in the water−CA system on the water content. The total frequency shift of peak 1 (120 cm^{-1}) is as large as the red shift observed in the water to ice phase transition.[68] This comparison and the steady dependence of the red shift support the assertion that C═O···H−O−H interactions in the hydration shell constitute the main contribution to peak 1. As the droplet evaporates, the CA molecules, including the hydration shell, gain more proximity and may form water-bridged (CA−water−CA) liquid structures. In addition, the local cyclic (COOH···

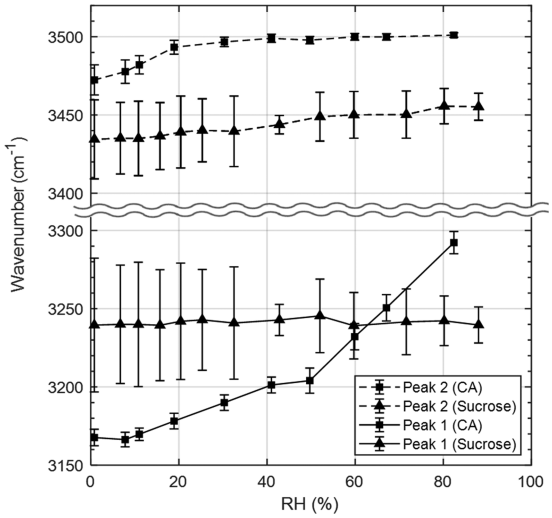

Figure 5. Frequency shifts of peak 1 and 2 for CA (squares) and sucrose (triangles) droplet versus RH. The lines are guides to the eyes. The error bars are expressed as 95% confidence intervals in the Gaussian fitting method.

https://dx.doi.org/10.1021/acs.jpcb.0c04919
J. Phys. Chem. B 2020, 124, 9385−9395

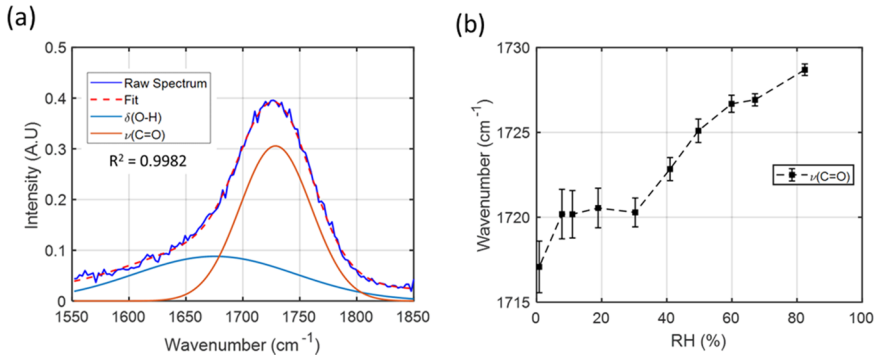

Figure 6. (a) Two-Gaussian fit of the 1550−1850 cm^{-1} region of the CA droplet at 82% RH. Here, the spectrum is deconvoluted with contributions from a broad water bending peak, δ(O−H), and a more strongly peaked carbonyl stretch, ν(C═O). (b) Upon the evaporation of the droplet, a red shift of the ν(C═O) peak was observed. A full table of the fitting parameters is given in Supporting Information, Table S4.

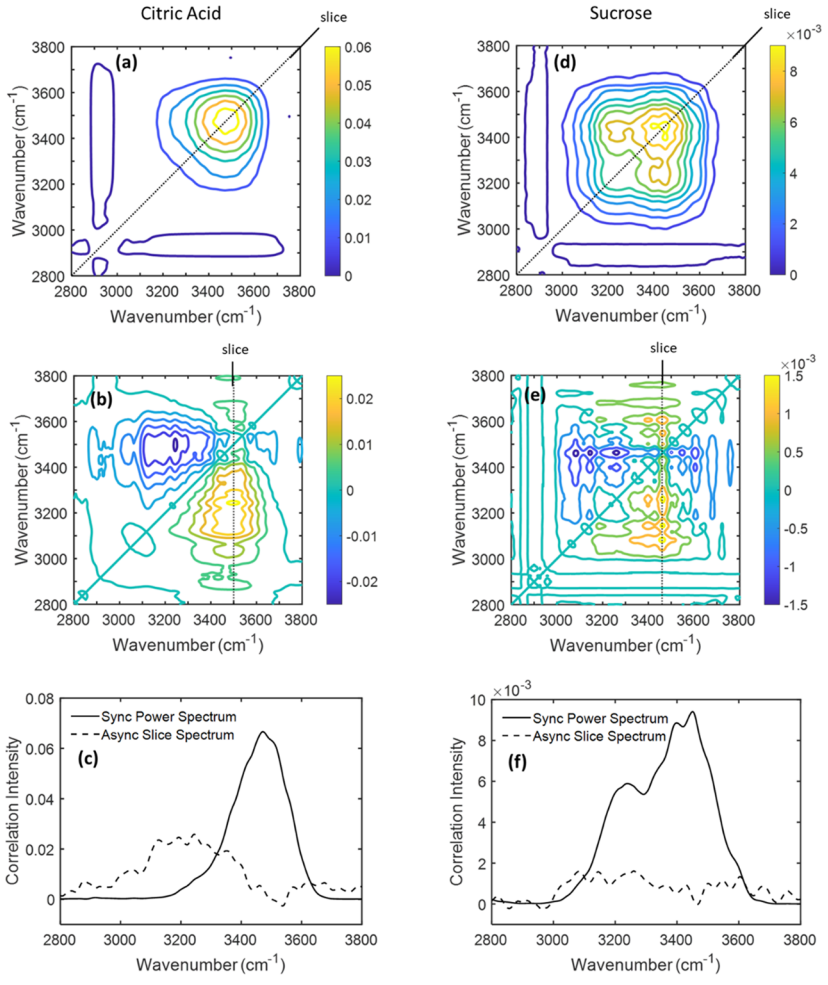

Figure 7. 2DCOS of CA and the sucrose droplets. On the left side of the frame, the synchronous spectrum (a), asynchronous spectrum (b), and slice spectra (c) are shown for a CA droplet. The synchronous spectrum (d), asynchronous spectrum (e), and slice spectra (f) for a sucrose droplet are placed on the right side. For the synchronous spectra (a) and (d), all correlation intensity values are positive. In the asynchronous spectra (b) and (e), the yellow and blue lines represent positive and negative correlation intensities, respectively. The raw spectra were smoothed before 2D analysis until the noise diminished.

HOOC) interaction of CA−CA can appear in such high solute concentration.[55] The strength of C═O···H−O hydrogen bond between cyclic CA−CA interaction is even stronger than that of COOH−water, and the accompanied shift in the ν(O−H) frequency can be observed at the spectral region of peak 1 (3000−3200 cm^{-1}).[60] This increased probability for these strong interactions may lead to the substantial monotonic red shift of peak 1 in CA droplets. Therefore, not only the increasing probability of CA−water contributes to the large red shift of peak 1, but also the augmenting number of events in COOH···HOOC interactions plays an important part, as the evaporation of the droplet continues. These changes in overall hydrogen-bond interactions and their spectral contribution can explain the peculiar red shift (120 cm^{-1}) of peak 1.

https://dx.doi.org/10.1021/acs.jpcb.0c04919
J. Phys. Chem. B 2020, 124, 9385−9395

On the other hand, the rapid red shift of peak 2 below RH ~20% suggests that weaker hydrogen-bond interactions are mainly affected at low RH, unlike peak 1 (strong interaction). These observations on peak shifts draw the general molecular picture of hydrogen-bond evolution in the supersaturated CA−water system under continuous evaporation: the CA molecules form a water-bridged complex liquid structure early and the remaining water molecules start being incorporated with the structure. This decoupling behavior of strong and weak interactions in the CA droplet will be discussed in detail using a 2D correlation analysis in the later section.

In the case of the sucrose droplet, the frequency shift of peak 1 is negligible considering the uncertainty of peak position determination using the Gaussian deconvolution. Unlike CA, the molecular structure of sucrose does not favor the formation of strongly bound water-bridged structures given the more weakly hydrogen-bonded hydroxyl groups that are involved. This is consistent with the absence of a pronounced red shift of peak 1 in sucrose. For the weaker hydrogen bonds (peak 2), sucrose droplets exhibit a linear red shift of about ~18 cm^{-1} over the evaporation. This red shift may be caused by increased hydrogen-bond interactions as the mobility of water molecules decreases. According to the calculation with the kinetic multilayer model, the sucrose droplet formed a glassy outer shell and the rate of equilibration of the droplet dramatically decreases below 50% RH (Figure S1). Thus, the frequency shift of peak 1 and 2 at this nonequilibrium RH region showed minimal variation considering large uncertainty (Figure 5). Overall, in the sucrose droplets, the strengthening of hydrogen-bond interactions as shown by the red shift of peak 2 (18 cm^{-1}) is minor compared to the red shift of the CA droplets (peak 1: 120 cm^{-1}, peak 2: 30 cm^{-1}).

In addition to the frequency shift of the ν(O−H) band, the evolution of the C═O stretch (~1730 cm^{-1}) and O−H bending (~1650 cm^{-1}) modes are demonstrated using a two-Gaussian analysis in Figure 6. Along with the decrease in RH, cyclic hydrogen-bond interactions between carboxyl groups (COOH···HOOC) intensify as the CA molecules gain more proximity as well as the CA−water−CA interaction. These growing interactions lead to the red shift of the ν(C═O) peak, as shown in Figure 6b. The trend in the red shift of the ν(C═O) peak is qualitatively more similar to peak 1 than peak 2 in Figure 5. This similarity strengthens the argument that the main contribution to peak 1 in the CA droplets is the strong CA−water interaction within the first hydration shell.

3.4. 2D Correlation Raman Spectroscopy (2DCOS). 2D correlation spectroscopy is a powerful analytical method, especially for comparing multiple spectra with physical or chemical perturbations.[36] In the present study, dehydration through the reduction in the ambient RH is the perturbation for the system, and the 2D correlation Raman spectra (2DCOS) of aqueous CA and sucrose droplets provide insights into the nature of that perturbation independent of the linear spectra presented above. In what follows, the synchronous and asynchronous 2D correlation spectra for CA and sucrose aqueous droplets are presented.

In the 2D synchronous spectrum, simultaneous or coincidental changes of spectral intensities at ν_1 and ν_2 appear as diagonal autopeaks and cross peaks, which are symmetric with respect to the diagonal axis. When a certain region of the spectra exhibits greater intensity changes as a function of the perturbation, a strong diagonal autopeak appears in that region. Cross peaks emerge in off-diagonal positions when simultaneous spectral changes occur at two different frequencies. A significant cross peak provides evidence for the possibility of a coupled or related origin for the spectral variations at different frequencies. In the 2D asynchronous spectrum, only off-diagonal and antisymmetric cross peaks appear. A significant asynchronous cross peak indicates that two dynamic changes in spectral intensities are occurring as a function of the perturbation, and that they vary out of phase with each other. The sign of an asynchronous cross peak is positive when the intensity change at ν_1 occurs before ν_2 as the perturbation progresses, and it is negative if the change at ν_1 occurs after ν_2 in the ordered progression of changing external perturbation.

Figure 7 shows the 2DCOS for the CA (RH = 67−1%) and sucrose (RH = 60−1%) droplets. The frequencies (in wavenumbers) of the peaks observed in the synchronous and asynchronous spectra are given in Table 1. In the 2DCOS of

Table 1. Peak Positions (cm^{-1}) Determined by 2DCOS Analysis in the ν(O−H) Vibrational Band

citric acid		sucrose	
synchronous	asynchronous	synchronous	asynchronous
3475	3500	3450	
	3250	3235	

the CA droplet, only a strong autopeak at (3475, 3475 cm^{-1}) is evident in the synchronous spectrum (Figure 7a). Except for the minor peak at ~2900 cm^{-1} (negligible correlation between O−H and C−H), there is no off-diagonal correlation peak. Figure 7c shows the power spectrum (diagonal slice) generated from the synchronous spectrum. From the power spectrum, it can be inferred that most of the spectral intensity variance takes place near 3500 cm^{-1}. For the asynchronous spectrum (Figure 7b), strong asynchronicity near (3500, 3250 cm^{-1}) is observed and the corresponding slice spectrum is shown in Figure 7c. The presence of the asynchronous peak near (3500, 3250 cm^{-1}) informs that the intensity changes in the two frequency regions are out-of-phase, implying that there are different kinds of interactions. The metastable CA−water system is not a simple two-component system; otherwise, the asynchronous spectrum would not generate any peak. This asynchronicity and the absence of the synchronous cross peak in the CA droplet supports the hypothesis that there are different origins for the two peaks (~3250 and ~3500 cm^{-1}) along with the frequency shifts discussed in the previous section. It should be noted that not every spectral feature of the two peaks is due to the strong interaction (CA−water and CA−CA in the hydration shell) and weak interaction (water−water interaction outside the hydration shell). The overlapping ν(C−H) peak and hydroxyl ν(O−H) from CA make minor contributions to the intensity of peak 1. To elucidate the intermolecular interactions in detail, information beyond the band positions of the vibrational spectra is necessary.

2DCOS of the sucrose droplet shows distinct features compared to 2DCOS of the CA droplets. The synchronous spectrum of the sucrose droplet (Figure 7d) features two overlapping autopeaks near 3235 and 3450 cm^{-1} as well as a positive cross peak at (3235, 3450 cm^{-1}). The position of this cross peak corresponds with the initial assignment of strong and weak hydrogen-bond interactions. The diagonal picture of the synchronous spectrum is explicitly shown in the power spectrum in Figure 7f. Unlike the case of the CA droplet, the

https://dx.doi.org/10.1021/acs.jpcb.0c04919
J. Phys. Chem. B 2020, 124, 9385−9395

existence of a synchronous cross peak indicates that the spectral intensity changes at 3235 and 3450 cm^{-1} are correlated. Moreover, no significant spectral information can be obtained from the asynchronous spectra (Figure 7e). The slice spectrum at the highest correlation intensity (3460 cm^{-1}) shows small asynchronicity near 3100 cm^{-1} in Figure 7f, but this band is indiscernible from the noise-like feature. The overall interpretation of the 2DCOS of the sucrose droplet further strengthens the supposition that the strong and weak hydrogen interactions in this system are correlated with each other and the ν(O−H) spectral features share a common origin (intertwined H−O···H−O interactions of sucrose−sucrose, sucrose−water, and water−water).

Up to this point, 2DCOS on the CA and the sucrose droplet has provided considerable information on the dynamic behavior of the Raman spectra. The peak assignments from the earlier section and the positions of the synchronous and asynchronous cross peaks of each system manifest excellent agreement. This consistency provides support for the conclusion that in the CA droplets strong (CA−CA and CA−water) and weak (water−water) interactions are not associated, while in the sucrose droplets both strong and weak interactions share the same origin. Even the simple observation that the synchronous and asynchronous spectra of both systems demonstrate contrasting patterns reveals that the different functional groups of the solute molecules govern the characters of hydrogen-bond interactions, especially in the metastable liquid system.

4. DISCUSSION

The significant difference in the extent of strong and weak hydrogen-bond interactions in CA versus sucrose can explain the peculiar behaviors of the corresponding droplets in their metastable states. First, it must be noted that the viscosity of sucrose droplets is 4−9 orders of magnitude higher than the CA droplets in the range of RH = 10−50%.[69] According to the studies on the relationship between hydrogen bond and viscosity by Okada et al., the strength of hydrogen bond is not the main factor that affects viscosity.[47] Instead, our in-depth spectroscopic analysis on the CA and the sucrose droplet suggests that the large difference in the viscosity between the two systems is due to the characteristic hydrogen-bond structure of the solutions. As shown in the asynchronous spectrum of CA (Figure 7b), the strong hydrogen-bond interactions within the hydration shell and the weak interactions change at different rates. For the sucrose droplet, it was argued that the evident correlation between strong and weak interaction might lead water and sucrose to be intertwined through hydrogen bond and form a network-like liquid structure. This divergence in correlated intermolecular behavior may give rise to the orders of magnitudes lower viscosity of CA compared to the sucrose. NMR studies on the viscosity of organic acids in the alcohol/water system support this hypothesis by reporting that the change in viscosity is due to the long-range interaction between the nonadjacent molecular segments.[70] Strong long-range interactions mentioned in this study may correspond to the network-like liquid structure of the sucrose droplet. The viscosity of OAs is analyzed and predicted using the O/C ratio or the types and the number of the functional groups of the organic molecules.[71,72] In addition to these methods, the results from this study suggest that investigating hydrogen-bond dynamics can provide valuable insights to the viscosity of OAs, especially for the aqueous droplets.

In addition, a previous study measuring diffusion coefficients of water (D_w) using H_2O/D_2O exchange from this laboratory presented evidence for significant inhibition of water diffusion in the CA droplets at RH below 15%, while the sucrose droplets showed slow but complete diffusion.[11] To account for an incomplete exchange of H_2O to D_2O in the CA droplets, a parameter χ ($0 < \chi < 1$) to represent the asymptotic isotope exchange fraction was adopted. For example, at 8% RH, the H_2O/D_2O exchange of the droplet was found to be ∼82% complete ($\chi = 0.82$), and the measured D_w value was 2.45×10^{-15} m^2 s^{-1}. In contrast, the sucrose droplets showed complete H_2O/D_2O exchange at 26% RH, where the measured value of D_w was nearly an order of magnitude lower (4.52×10^{-16} m^2 s^{-1}) than the case of incomplete diffusion in the CA droplet at RH 8%.[11] This distinctive behavior of a limitation of water diffusion in the metastable CA droplets was attributed to the strong hydrogen-bond interactions, leading to the formation of local water-bridged CA−water−CA oligomer liquid structures. The result of Raman 2DCOS presented here adds more evidence to the hypothesis that inhibition of diffusion is caused by strong hydrogen-bond structures, and these metastable liquid structures lead to a significant internal barrier for diffusion of water within the droplet. The diffusion inhibition has been observed by others and our study sheds light on the fundamental cause of the phenomenon.[7,73]

It is counterintuitive that the CA droplets with lower viscosity show diffusion inhibition compared to the sucrose droplets with much higher viscosity. However, from the result of the ν(O−H) frequency shift of the CA droplet, it is plausible that the stronger hydrogen-bond interaction may lead to trapping and immobilization of the water molecules around the CA molecules. In other words, the primary reason for apparent incomplete H_2O/D_2O exchange of the CA droplet below 15% RH described in the previous paper is the thermodynamic limitation of water diffusion caused by the strong hydrogen bonds. It is well known that the common form of the CA crystal in the ambient condition is a monohydrated structure.[74] Similar to the hydrated crystal structure, the highly supersaturated CA droplets may have a water-bridged solute liquid structure, and this can be the cause of the diffusion inhibition of water.

A final point worth noting is that the intensity distribution of the exciting laser within the heterogeneous droplets in this size range is not homogeneous because the steep refractive index gradient between the outer and inner regions causes the light to be focused in particular regions.[75,76] This effect will influence the spectral probe region as the droplets dry and form shell-core structures. In particular, in the dry particle case, the Raman spectra will be more representative of the chemical composition of the outer shell rather than the inside core of the droplets. The exploitation of this effect is beyond the scope of the present work but may prove useful in future studies of the heterogeneous droplets.

5. CONCLUSIONS

In situ Raman observations on single aqueous CA and sucrose droplets in the ν(O−H) region over the RH range of 1−88% exhibit changes in the hydrogen-bond structures, which are related to the differences in the functional groups of these solutes. Gaussian deconvolution of the Raman spectra allowed examination of the spectral reconstruction of the weak and

https://dx.doi.org/10.1021/acs.jpcb.0c04919
J. Phys. Chem. B 2020, 124, 9385−9395

strong hydrogen-bond regions. The Raman spectra were analyzed using 2DCOS, showing the decoupling of the strong and weak hydrogen bonds for the CA droplet and correlation for the sucrose droplets at a high level of solute supersaturation. The distinctive macroscopic properties of supersaturated OOAs such as viscosity and water diffusion can be governed by the liquid structures, as demonstrated in the intensity ratio of the strong and weak hydrogen-bond peaks. The use of the environment-controlled EDB system in this case allows access to extreme solute supersaturation states of model OOAs and their Raman spectroscopic analysis. These measurements have provided valuable insights into the evolution of the hydrogen-bond structures and the molecular origin of nontrivial physical properties of metastable or glassy state OOAs. Further studies include spectral analysis of the temperature effect on these droplets, possibly providing more quantitative information on the energetics and dynamics of hydrogen-bond interactions in OOAs.

■ ASSOCIATED CONTENT

Supporting Information

The Supporting Information is available free of charge at https://pubs.acs.org/doi/10.1021/acs.jpcb.0c04919.

Solute supersaturation ratio versus RH, full Gaussian fitting parameters, and Mie scattering images (PDF)

■ AUTHOR INFORMATION

Corresponding Author

Robert E. Continetti − *Department of Chemistry and Biochemistry, University of California San Diego, La Jolla, California 92093-0340, United States;* orcid.org/0000-0002-0685-4459; Email: rcontinetti@ucsd.edu

Authors

Pyeongeun Kim − *Department of Chemistry and Biochemistry, University of California San Diego, La Jolla, California 92093-0340, United States*

Wei Xiong − *Department of Chemistry and Biochemistry, University of California San Diego, La Jolla, California 92093-0340, United States;* orcid.org/0000-0002-7702-0187

Complete contact information is available at: https://pubs.acs.org/10.1021/acs.jpcb.0c04919

Author Contributions

The manuscript was written through the contributions of all authors. All authors have given approval to the final version of the manuscript.

Notes

The authors declare no competing financial interest.

■ ACKNOWLEDGMENTS

This work was supported by the NSF through the NSF Center for Aerosol Impacts on Chemistry of the Environment (CAICE), CHE-1801971. We thank the reviewers for the insightful comments. All relevant data will be made available online at the CAICE UC San Diego Library Digital Collections (https://doi.org/10.6075/J0DZ06T2).

■ REFERENCES

(1) Seinfeld, J. H.; Pandis, S. N. *Atmospheric Chemistry and Physics: From Air Pollution to Climate Change*; John Wiley & Sons, 2016.

(2) Shiraiwa, M.; Ueda, K.; Pozzer, A.; Lammel, G.; Kampf, C. J.; Fushimi, A.; Enami, S.; Arangio, A. M.; Fröhlich-Nowoisky, J.; Fujitani, Y.; et al. Aerosol Health Effects from Molecular to Global Scales. *Environ. Sci. Technol.* **2017**, *51*, 13545−13567.

(3) Knibbs, L. D.; Johnson, G. R.; Kidd, T. J.; Cheney, J.; Grimwood, K.; Kattenbelt, J. A.; O'Rourke, P. K.; Ramsay, K. A.; Sly, P. D.; Wainwright, C. E.; et al. Viability of Pseudomonas Aeruginosa in Cough Aerosols Generated by Persons with Cystic Fibrosis. *Thorax* **2014**, *69*, 740−745.

(4) van Doremalen, N.; Bushmaker, T.; Morris, D. H.; Holbrook, M. G.; Gamble, A.; Williamson, B. N.; Tamin, A.; Harcourt, J. L.; Thornburg, N. J.; Gerber, S. I.; et al. Aerosol and Surface Stability of SARS-CoV-2 as Compared with SARS-CoV-1. *N. Engl. J. Med.* **2020**, *382*, 1564−1567.

(5) Prather, K. A.; Wang, C. C.; Schooley, R. T. Reducing Transmission of SARS-CoV-2. *Science* **2020**, *368*, 1422−1424.

(6) Rood, M. J.; Shaw, M. A.; Larson, T. V.; Covert, D.S. Ubiquitous Nature of Ambient Metastable Aerosol. *Nature* **1989**, *337*, 537−539.

(7) Zobrist, B.; Marcolli, C.; Pedernera, D. A.; Koop, T. Do Atmospheric Aerosols Form Glasses? *Atmos. Chem. Phys.* **2008**, *8*, 5221−5244.

(8) Shiraiwa, M.; Li, Y.; Tsimpidi, A. P.; Karydis, V. A.; Berkemeier, T.; Pandis, S. N.; Lelieveld, J.; Koop, T.; Pöschl, U. Global Distribution of Particle Phase State in Atmospheric Secondary Organic Aerosols. *Nat. Commun.* **2017**, *8*, No. 15002.

(9) Pankow, J. F. An Absorption Model of the Gas/Aerosol Partitioning Involved in the Formation of Secondary Organic Aerosol. *Atmos. Environ.* **1994**, *28*, 189−193.

(10) Freedman, M. A. Phase Separation in Organic Aerosol. *Chem. Soc. Rev.* **2017**, *46*, 7694−7705.

(11) Nadler, K. A.; Kim, P.; Huang, D.-L.; Xiong, W.; Continetti, R. E. Water Diffusion Measurements of Single Charged Aerosols Using H_2O/D_2O Isotope Exchange and Raman Spectroscopy in an Electrodynamic Balance. *Phys. Chem. Chem. Phys.* **2019**, *21*, 15062−15071.

(12) Davies, J. F.; Wilson, K. R. Nanoscale Interfacial Gradients Formed by the Reactive Uptake of OH Radicals onto Viscous Aerosol Surfaces. *Chem. Sci.* **2015**, *6*, 7020−7027.

(13) Bones, D. L.; Reid, J. P.; Lienhard, D. M.; Krieger, U. K. Comparing the Mechanism of Water Condensation and Evaporation in Glassy Aerosol. *Proc. Natl. Acad. Sci. U.S.A.* **2012**, *109*, 11613−11618.

(14) Zobrist, B.; Soonsin, V.; Luo, B. P.; Krieger, U. K.; Marcolli, C.; Peter, T.; Koop, T. Ultra-Slow Water Diffusion in Aqueous Sucrose Glasses. *Phys. Chem. Chem. Phys.* **2011**, *13*, 3514−3526.

(15) Jimenez, J. L.; Canagaratna, M. R.; Donahue, N. M.; Prevot, A. S. H.; Zhang, Q.; Kroll, J. H.; DeCarlo, P. F.; Allan, J. D.; Coe, H.; Ng, N. L.; et al. Evolution of Organic Aerosols in the Atmosphere. *Science* **2009**, *326*, 1525−1529.

(16) Zhao, J.; Khalizov, A.; Zhang, R.; McGraw, R. Hydrogen-Bonding Interaction in Molecular Complexes and Clusters of Aerosol Nucleation Precursors. *J. Phys. Chem. A* **2009**, *113*, 680−689.

(17) Walrafen, G. E. Raman Spectral Studies of Water Structure. *J. Chem. Phys.* **1964**, *40*, 3249−3256.

(18) Goy, C.; Potenza, M. A. C.; Dedera, S.; Tomut, M.; Guillerm, E.; Kalinin, A.; Voss, K. O.; Schottelius, A.; Petridis, N.; Prosvetov, A.; et al. Shrinking of Rapidly Evaporating Water Microdroplets Reveals Their Extreme Supercooling. *Phys. Rev. Lett.* **2018**, *120*, No. 015501.

(19) Segtnan, V. H.; Šašić, Š.; Isaksson, T.; Ozaki, Y. Studies on the Structure of Water Using Two-Dimensional near-Infrared Correlation Spectroscopy and Principal Component Analysis. *Anal. Chem.* **2001**, *73*, 3153−3161.

(20) Vollmar, P. M. Ionic Interactions in Aqueous Solution: A Raman Spectral Study. *J. Chem. Phys.* **1963**, *39*, 2236−2248.

(21) Liu, D.; Ma, G.; Levering, L. M.; Allen, H. C. Vibrational Spectroscopy of Aqueous Sodium Halide Solutions and Air−Liquid Interfaces: Observation of Increased Interfacial Depth. *J. Phys. Chem. B* **2004**, *108*, 2252−2260.

(22) Ahmed, M.; Namboodiri, V.; Singh, A. K.; Mondal, J. A.; Sarkar, S. K. How Ions Affect the Structure of Water: A Combined Raman Spectroscopy and Multivariate Curve Resolution Study. *J. Phys. Chem. B* **2013**, *117*, 16479−16485.
(23) Dolenko, T. A.; Burikov, S. A.; Dolenko, S. A.; Efitorov, A. O.; Plastinin, I. V.; Yuzhakov, V. I.; Patsaeva, S. V. Raman Spectroscopy of Water-Ethanol Solutions: The Estimation of Hydrogen Bonding Energy and the Appearance of Clathrate-like Structures in Solutions. *J. Phys. Chem. A* **2015**, *119*, 10806−10815.
(24) Bogdan, A.; Molina, M. J.; Tenhu, H.; Loerting, T. Multiple Glass Transitions and Freezing Events of Aqueous Citric Acid. *J. Phys. Chem. A* **2015**, *119*, 4515−4523.
(25) Dette, H. P.; Koop, T. Glass Formation Processes in Mixed Inorganic/Organic Aerosol Particles. *J. Phys. Chem. A* **2015**, *119*, 4552−4561.
(26) Lienhard, D. M.; Bones, D. L.; Zuend, A.; Krieger, U. K.; Reid, J. P.; Peter, T. Measurements of Thermodynamic and Optical Properties of Selected Aqueous Organic and Organic-Inorganic Mixtures of Atmospheric Relevance. *J. Phys. Chem. A* **2012**, *116*, 9954−9968.
(27) Ashkin, A. Acceleration and Trapping of Particles by Radiation Pressure. *Phys. Rev. Lett.* **1970**, *24*, 156−159.
(28) Dennis-Smither, B. J.; Marshall, F. H.; Miles, R. E. H.; Preston, T. C.; Reid, J. P. Volatility and Oxidative Aging of Aqueous Maleic Acid Aerosol Droplets and the Dependence on Relative Humidity. *J. Phys. Chem. A* **2014**, *118*, 5680−5691.
(29) Cai, C.; Stewart, D. J.; Reid, J. P.; Zhang, Y. H.; Ohm, P.; Dutcher, C. S.; Clegg, S. L. Organic Component Vapor Pressures and Hygroscopicities of Aqueous Aerosol Measured by Optical Tweezers. *J. Phys. Chem. A* **2015**, *119*, 704−718.
(30) Davies, J. F.; Wilson, K. R. Raman Spectroscopy of Isotopic Water Diffusion in Ultraviscous, Glassy, and Gel States in Aerosol by Use of Optical Tweezers. *Anal. Chem.* **2016**, *88*, 2361−2366.
(31) Davis, E. J. A History of Single Aerosol Particle Levitation. *Aerosol Sci. Technol.* **1997**, *26*, 212−254.
(32) Tong, H. J.; Ouyang, B.; Nikolovski, N.; Lienhard, D. M.; Pope, F. D.; Kalberer, M. A New Electrodynamic Balance (EDB) Design for Low-Temperature Studies: Application to Immersion Freezing of Pollen Extract Bioaerosols. *Atmos. Meas. Tech.* **2015**, *8*, 1183−1195.
(33) Miles, R. E. H.; Davies, J. F.; Reid, J. P. The Influence of the Surface Composition of Mixed Monolayer Films on the Evaporation Coefficient of Water. *Phys. Chem. Chem. Phys.* **2016**, *18*, 19847−19858.
(34) Darvas, M.; Picaud, S.; Jedlovszky, P. Molecular Dynamics Simulations of the Water Adsorption around Malonic Acid Aerosol Models. *Phys. Chem. Chem. Phys.* **2013**, *15*, 10942−10951.
(35) Noda, I. Generalized Two-Dimensional Correlation Method Applicable to Infrared, Raman, and Other Types of Spectroscopy. *Appl. Spectrosc.* **1993**, *47*, 1329−1336.
(36) Noda, I. Advances in Two-Dimensional Correlation Spectroscopy (2DCOS). *Front. Adv. Mol. Spectrosc.* **2017**, *54*, 47−75.
(37) Paul, W. Electromagnetic Traps for Charged and Neutral Particles (Nobel Lecture). *Angew. Chem., Int. Ed.* **1990**, *29*, 739−748.
(38) Trevitt, A. J.; Wearne, P. J.; Bieske, E. J. Calibration of a Quadrupole Ion Trap for Particle Mass Spectrometry. *Int. J. Mass Spectrom.* **2007**, *262*, 241−246.
(39) Shinohara, H.; Yamakita, Y.; Ohno, K. Raman Spectra of Polycyclic Aromatic Hydrocarbons. Comparison of Calculated Raman Intensity Distributions with Observed Spectra for Naphthalene, Anthracene, Pyrene, and Perylene. *J. Mol. Struct.* **1998**, *442*, 221−234.
(40) Glantschnig, W. J.; Chen, S.-H. Light Scattering from Water Droplets in the Geometrical Optics Approximation. *Appl. Opt.* **1981**, *20*, 2499.
(41) Graßmann, A.; Peters, F. Size Measurement of Very Small Spherical Particles by Mie Scattering Imaging (MSI). *Part. Part. Syst. Charact.* **2004**, *21*, 379−389.
(42) Rzesanke, D.; Nadolny, J.; Duft, D.; Muller, R.; Kiselev, A.; Leisner, T. On the Role of Surface Charges for Homogeneous Freezing of Supercooled Water Microdroplets. *Phys. Chem. Chem. Phys.* **2012**, *14*, 9359−9363.
(43) Hermann, G.; Zhang, Y.; Wassermann, B.; Fischer, H.; Quennet, M.; Ruhl, E. Charge Effects on the Efflorescence in Single Levitated Droplets. *J. Phys. Chem. A* **2017**, *121*, 6790−6799.
(44) Hu, Q.; Zhao, H.; Ouyang, S. Understanding Water Structure from Raman Spectra of Isotopic Substitution H_2O/D_2O up to 573 K. *Phys. Chem. Chem. Phys.* **2017**, *19*, 21540−21547.
(45) Smith, J. D.; Cappa, C. D.; Wilson, K. R.; Cohen, R. C.; Geissler, P. L.; Saykally, R. J. Unified Description of Temperature-Dependent Hydrogen-Bond Rearrangements in Liquid Water. *Proc. Natl. Acad. Sci. U.S.A.* **2005**, *102*, 14171−14174.
(46) Kojima, S. Anomalous Behaviour of the O-H Stretching Vibrational Mode in the Liquid-Glass Transition of Glycerol. *J. Mol. Struct.* **1993**, *294*, 193−195.
(47) Okada, T.; Komatsu, K.; Kawamoto, T.; Yamanaka, T.; Kagi, H. Pressure Response of Raman Spectra of Water and Its Implication to the Change in Hydrogen Bond Interaction. *Spectrochim. Acta, Part A* **2005**, *61*, 2423−2427.
(48) Palombo, F.; Paolantoni, M.; Sassi, P.; Morresi, A.; Cataliotti, R. S. Spectroscopic Studies of the "Free" OH Stretching Bands in Liquid Alcohols. *J. Mol. Liq.* **2006**, *125*, 139−146.
(49) Pershin, S. M.; Bunkin, A. F.; Lukyanchenko, V. A.; Nigmatullin, R. R. Detection of the OH Band Fine Structure in Liquid Water by Means of New Treatment Procedure Based on the Statistics of the Fractional Moments. *Laser Phys. Lett.* **2007**, *4*, 809−813.
(50) Ikushima, Y.; Hatakeda, K.; Saito, N.; Arai, M. An in Situ Raman Spectroscopy Study of Subcritical and Supercritical Water: The Peculiarity of Hydrogen Bonding near the Critical Point. *J. Chem. Phys.* **1998**, *108*, 5855−5860.
(51) Carey, D. M.; Korenowski, G. M. Measurement of the Raman Spectrum of Liquid Water. *J. Chem. Phys.* **1998**, *108*, 2669−2675.
(52) Burikov, S.; Dolenko, T.; Patsaeva, S.; Starokurov, Y.; Yuzhakov, V. Raman and IR Spectroscopy Research on Hydrogen Bonding in Water-Ethanol Systems. *Mol. Phys.* **2010**, *108*, 2427−2436.
(53) Jung, Y. M.; Czarnik-Matusewicz, B.; Kim, S. B. Characterization of Concentration-Dependent Infrared Spectral Variations of Urea Aqueous Solutions by Principal Component Analysis and Two-Dimensional Correlation Spectroscopy. *J. Phys. Chem. B* **2004**, *108*, 13008−13014.
(54) Noda, I. Determination of Two-Dimensional Correlation Spectra Using the Hilbert Transform. *Appl. Spectrosc.* **2000**, *54*, 994−998.
(55) Chocholoušová, J.; Vacek, J.; Hobza, P. Acetic Acid Dimer in the Gas Phase, Nonpolar Solvent, Microhydrated Environment, and Dilute and Concentrated Acetic Acid: Ab Initio Quantum Chemical and Molecular Dynamics Simulations. *J. Phys. Chem. A* **2003**, *107*, 3086−3092.
(56) Wang, H.; Chen, W.; Wagner, J. C.; Xiong, W. Local Ordering of Lattice Self-Assembled SDS@2β-CD Materials and Adsorbed Water Revealed by Vibrational Sum Frequency Generation Microscope. *J. Phys. Chem. B* **2019**, *123*, 6212−6221.
(57) Nakabayashi, T.; Kosugi, K.; Nishi, N. Liquid Structure of Acetic Acid Studied by Raman Spectroscopy and Ab Initio Molecular Orbital Calculations. *J. Phys. Chem. A* **1999**, *103*, 8595−8603.
(58) Tonannavar, J.; Chavan, Y. B.; Yenagi, J. A Study of Hydrogen Bonded Vibrational Spectra of (R)-(+)-Methylsuccinic Acid, as Aided by DFT Dimer Analysis. *Spectrochim. Acta, Part A* **2016**, *160*, 19−25.
(59) Ng, J. B.; Shurvell, H. F. Application of Factor Analysis and Band Contour Resolution Techniques to the Raman Spectra of Acetic Acid in Aqueous Solution. *J. Phys. Chem. A.* **1987**, *91*, 496−500.
(60) Bhattacharjee, R.; Jain, Y. S.; Bist, H. D. Laser Raman and Infrared Spectra of Tartaric Acid Crystals. *J. Raman Spectrosc.* **1989**, *20*, 91−97.
(61) Desiraju, G. R. Hydrogen Bridges in Crystal Engineering: Interactions without Borders. *Acc. Chem. Res.* **2002**, *35*, 565−573.

https://dx.doi.org/10.1021/acs.jpcb.0c04919
J. Phys. Chem. B 2020, 124, 9385−9395

(62) Ebisuzaki, Y.; Angel, S. M. Raman Study of Hydrogen Bonding in α and B-oxalic Acid Dihydrate. *J. Raman Spectrosc.* **1981**, *11*, 306−311.
(63) Nishikawa, K.; Iijima, T. Small-Angle X-Ray Scattering Study of Fluctuations in Ethanol and Water Mixtures. *J. Phys. Chem. B.* **1993**, *97*, 10824−10828.
(64) Mohaček-Grošev, V.; Grdadolnik, J.; Stare, J.; Hadži, D. Identification of Hydrogen Bond Modes in Polarized Raman Spectra of Single Crystals of α-Oxalic Acid Dihydrate. *J. Raman Spectrosc.* **2009**, *40*, 1605−1614.
(65) Peng, C.; Chan, M. N.; Chan, C. K. The Hygroscopic Properties of Dicarboxylic and Multifunctional Acids: Measurements and UNIFAC Predictions. *Environ. Sci. Technol.* **2001**, *35*, 4495−4501.
(66) Yalkowsky, S. H.; He, Y.; Jain, P. *Handbook of Aqueous Solubility Data*, 2nd ed.; CRC Press Inc., 2010.
(67) Lienhard, D. M.; Huisman, A. J.; Bones, D. L.; Te, Y. F.; Luo, B. P.; Krieger, U. K.; Reid, J. P. Retrieving the Translational Diffusion Coefficient of Water from Experiments on Single Levitated Aerosol Droplets. *Phys. Chem. Chem. Phys.* **2014**, *16*, 16677−16683.
(68) Xue, X.; He, Z. Z.; Liu, J. Detection of Water-Ice Phase Transition Based on Raman Spectrum. *J. Raman Spectrosc.* **2013**, *44*, 1045−1048.
(69) Song, Y. C.; Haddrell, A. E.; Bzdek, B. R.; Reid, J. P.; Bannan, T.; Topping, D. O.; Percival, C.; Cai, C. Measurements and Predictions of Binary Component Aerosol Particle Viscosity. *J. Phys. Chem. A* **2016**, *120*, 8123−8137.
(70) Miyamoto, T.; Cantow, H.-J. A Nuclear Magnetic Resonance Study on the Conformation and Molecular Interaction of Polyelectrolyte Model Compound in Alcohol/Water Mixtures. *Makromol. Chem.* **1973**, *169*, 211−218.
(71) Marsh, A.; Rovelli, G.; Song, Y. C.; Pereira, K. L.; Willoughby, R. E.; Bzdek, B. R.; Hamilton, J. F.; Orr-Ewing, A. J.; Topping, D. O.; Reid, J. P. Accurate Representations of the Physicochemical Properties of Atmospheric Aerosols: When Are Laboratory Measurements of Value? *Faraday Discuss.* **2017**, *200*, 639−661.
(72) Rothfuss, N. E.; Marsh, A.; Rovelli, G.; Petters, M. D.; Reid, J. P. Condensation Kinetics of Water on Amorphous Aerosol Particles. *J. Phys. Chem. Lett.* **2018**, *9*, 3708−3713.
(73) Tong, H. J.; Reid, J. P.; Bones, D. L.; Luo, B. P.; Krieger, U. K. Measurements of the Timescales for the Mass Transfer of Water in Glassy Aerosol at Low Relative Humidity and Ambient Temperature. *Atmos. Chem. Phys.* **2011**, *11*, 4739−4754.
(74) Caillet, A.; Rivoire, A.; Galvan, J. M.; Puel, F.; Fevotte, G. Crystallization of Monohydrate Citric Acid. 1. In Situ Monitoring through the Joint Use of Raman Spectroscopy and Image Analysis. *Cryst. Growth Des.* **2007**, *7*, 2080−2087.
(75) Bohren, C. F.; Huffman, D. R. *Absorption and Scattering of Light by Small Particles*; Wiley, 1998; Vol. *31*.
(76) Bastelberger, S.; Krieger, U. K.; Luo, B. P.; Peter, T. Time Evolution of Steep Diffusion Fronts in Highly Viscous Aerosol Particles Measured with Mie Resonance Spectroscopy. *J. Chem. Phys.* **2018**, *149*, 244506.

https://dx.doi.org/10.1021/acs.jpcb.0c04919
J. Phys. Chem. B 2020, 124, 9385−9395